

Accurate extraction of Lagrangian coherent structures over finite domains with application to flight data analysis over Hong Kong International Airport

Wenbo Tang,¹ Pak Wai Chan,² and George Haller^{3,a)}

¹*School of Mathematical and Statistical Sciences, Arizona State University, Tempe, Arizona 85287, USA*

²*Hong Kong Observatory, Hong Kong, China*

³*Department of Mechanical Engineering, McGill University, Montreal, Quebec H3A 2K6, Canada*

(Received 12 October 2009; accepted 29 November 2009; published online 5 January 2010)

Locating Lagrangian coherent structures (LCS) for dynamical systems defined on a spatially limited domain present a challenge because trajectory integration must be stopped at the boundary for lack of further velocity data. This effectively turns the domain boundary into an attractor, introduces edge effects resulting in spurious ridges in the associated finite-time Lyapunov exponent (FTLE) field, and causes some of the real ridges of the FTLE field to be suppressed by strong spurious ridges. To address these issues, we develop a finite-domain FTLE method that renders LCS with an accuracy and fidelity that is suitable for automated feature detection. We show the application of this technique to the analysis of velocity data from aircraft landing at the Hong Kong International Airport. © 2010 American Institute of Physics. [doi:10.1063/1.3276061]

Traditional approaches in the extraction of Lagrangian coherent structures (LCS) using finite-time Lyapunov exponents (FTLE) stop trajectories at the domain boundaries when data are only available in a limited region. This turns the domain boundaries into attractors and deteriorates the quality of the extraction. Direct application of this approach to practical problems is troublesome as spurious ridges appear and true ridges are suppressed, causing errors in the evaluation of a nonlinear flow field. In this paper we develop a new method that deals with this difficulty by extending the flow field into a linear global flow that best matches the data in the finite domain, and allows trajectories to continue to separate once they cross the domain boundaries. With the new scheme trajectory, separations previously stopped prematurely are now recovered with the separation rate locked at their exit values and the artificial attractors are removed.

I. INTRODUCTION

The accurate numerical or experimental detection of invariant manifolds requires the long-term tracking of trajectories. For instance, precise identification of an invariant manifold forming the tube of a hurricane requires the long-term integration of fluid particles. Since observational velocity data, as a rule, are only available on a spatial domain limited by the range of sensing instruments, individual particle integration will have to be stopped at the boundary of the domain.

Stopping trajectories at the boundary turns boundaries into attracting invariant manifolds, introducing spurious invariant structures into a LCS analysis (Refs. 3 and 5) of the data set. Specifically, repelling(attracting) boundaries will

show up as ridges of the forward(backward)-time FTLE field computed for the velocity field.

Stopping trajectories at the boundaries also introduces edge effects: trajectories tangent to the domain boundaries will stay inside the domain and continue onward whereas their neighbors will exit and stop. They, therefore, show up as ridges of the forward-time FTLE field, suggesting incorrectly the presence of repelling LCS in the flow (cf. discussions on Figs. 1 and 4). To make matters worse, actual ridges of the velocity field tend to get suppressed by these spurious ridges.

Reliable extraction of LCS will be crucially important if LCS extraction techniques were to be employed in real-time automated feature detection and decision making. An example where such reliability is critical is the ongoing effort to extract updrafts and downdrafts of airflows in real time near the flight paths of commercial aircraft near Hong Kong International Airport (HKIA) (see Sec. III below). Because remotely sensed velocity data are only available on a limited domain, an algorithm detecting air disturbances potentially hazardous for landing aircraft must not generate false alarms, and be able to highlight real disturbances with high precision.

In this paper, we show how a global smoothing technique borrowed from nonlinear analysis (Ref. 2) can be used to filter out spurious FTLE ridges and enhance real ones. We use the method of bump functions (or mollifiers) to extend the spatially confined velocity field consistently and smoothly to infinite domains. This approach—the finite-domain FTLE (FDFTLE) algorithm derived here—eliminates the creation of artificial structures and enhances the real LCS contained in the original domain.

Note that one can also try to compute the FTLE at a “cutoff” time when a trajectory leaves the domain. The stretching is normalized with the proper integration time.

^{a)}Electronic mail: george.haller@mcgill.ca.

However, there are difficulties associated with this approach. Aside from an obvious algorithmic complication and a shorter integration time leading to less distinguished trajectories, an additional issue arises due to the deformation of the flow. In order to compute for the FTLE, one needs to compute the gradient of the flow map, where a small neighborhood of an initial condition is considered. In extreme cases when neighboring trajectories all leave the domain earlier than the trajectory considered, the FTLE cannot be computed. As such, we only consider the FDFTLE method in this paper.

As an illustration, we show initial results on the application of the FDFTLE algorithm to analysis of velocity data from aircraft landing at HKIA. With FDFTLE, we are able to eliminate artificial ridges and identify a clear connection between the presence of certain types of LCS across landing paths and the occurrence of aborted landings.

II. THE FDFTLE ALGORITHM

A. Setup

Fluid particle motions in a two-dimensional (2D) incompressible flow satisfy

$$\dot{\mathbf{x}} = \mathbf{u}(\mathbf{x}, t), \quad \nabla \cdot \mathbf{u} = 0, \tag{1}$$

where $\mathbf{u}(\mathbf{x}, t) = (u_1(\mathbf{x}, t), u_2(\mathbf{x}, t))$ is assumed to be class C^1 in its spatial argument $\mathbf{x} = (x, y)$, and continuous in the time variable t . We will denote by $\mathbf{x}(t; t_0, \mathbf{x}_0)$ the position of a trajectory of Eq. (1) at time t , assuming that it started from the position \mathbf{x}_0 at time t_0 .

Assume that the velocity field $\mathbf{u}(\mathbf{x}, t)$ is only known over a rectangular spatial grid

$$\mathcal{G} = \{(x_i, y_j)\}_{i=1, \dots, m; j=1, \dots, n}.$$

Shifting the x and y coordinates if necessary, we may assume that \mathcal{G} is symmetric with respect to the origin of the (x, y) plane, i.e.,

$$x_i = -x_{m+1-i}, \quad y_j = -y_{n+1-j}, \quad i = 1, \dots, m; \quad j = 1, \dots, n. \tag{2}$$

Preserving the original definition of $\mathbf{u}(\mathbf{x}, t)$ on a large enough subset \mathcal{G}^0 of the grid \mathcal{G} , we would like to extend $\mathbf{u}(\mathbf{x}, t)$ smoothly to all of the (x, y) plane in a way such that the original ridges of the FTLE field

$$\sigma(t; t_0, \mathbf{x}_0) = \frac{1}{2|t - t_0|} \ln \left\{ \lambda_{\max} \left(\left[\frac{\partial \mathbf{x}(t; t_0, \mathbf{x}_0)}{\partial \mathbf{x}_0} \right]^T \frac{\partial \mathbf{x}(t; t_0, \mathbf{x}_0)}{\partial \mathbf{x}_0} \right) \right\} \tag{3}$$

computed for Eq. (1) are preserved within \mathcal{G}^0 under the extended velocity field $\mathbf{v}(\mathbf{x}, t)$. Preservation of the ridges in the extended velocity field will be ensured by the linearity of \mathbf{v} in the spatial variables \mathbf{x} outside the domain \mathcal{G} . Recall that the FTLE field associated with a linear vector field is constant, with its value converging to the largest Lyapunov exponent of the origin of the homogeneous part of the vector field.

B. Smooth extension outside the grid domain

The extension from \mathbf{u} to \mathbf{v} will involve the gradual deformation of the velocity field $\mathbf{u}(\mathbf{x}, t)$ starting from the boundary of the subset \mathcal{G}^0 up to the boundary of \mathcal{G} . The deformed velocity field will smoothly connect to a linear velocity field $\mathbf{v}_L(\mathbf{x}, t)$ defined globally outside \mathcal{G} . To minimize the deformation of \mathbf{u} over $\mathcal{G} - \mathcal{G}^0$, we select $\mathbf{v}_L(\mathbf{x}, t)$ to be the closest incompressible linear velocity field to $\mathbf{u}(\mathbf{x}, t)$ in the C^0 norm taken over the subgrid \mathcal{G} .

We first fix a small constant $\Delta > 0$ that will measure the distance between the boundaries of \mathcal{G} and a smaller rectangular grid $\mathcal{G}^0 \subset \mathcal{G}$. We will also use the averaging operation $\langle \cdot \rangle$ over \mathcal{G} defined for any scalar function $f(x, y, t)$,

$$\langle f \rangle = \frac{1}{m \times n} \sum_{i=1}^m \sum_{j=1}^n f(x_i, y_j). \tag{4}$$

We then have the following result.

Theorem 1:

(i) For any fixed time t , the velocity field

$$\mathbf{v}_L(\mathbf{x}, t) = \begin{pmatrix} \frac{\langle xu_1 - yu_2 \rangle}{\langle x^2 + y^2 \rangle} & \frac{\langle yu_1 \rangle}{\langle y^2 \rangle} \\ \frac{\langle xu_2 \rangle}{\langle x^2 \rangle} & \frac{\langle yu_2 - xu_1 \rangle}{\langle x^2 + y^2 \rangle} \end{pmatrix} \mathbf{x} + \begin{pmatrix} \langle u_1 \rangle \\ \langle u_2 \rangle \end{pmatrix} \tag{5}$$

is the closest linear, divergence-free velocity field to $\mathbf{u}(\mathbf{x}, t)$ in the C^0 norm over the grid \mathcal{G} .

(ii) A class C^1 extension [in $\mathbf{x} = (x, y)$] of the velocity field \mathbf{u} from \mathcal{G} to the whole (x, y) plane is given by

$$\mathbf{v} = \mathbf{v}_L + (\mathbf{u} - \mathbf{v}_L) \delta_x(|x|) \delta_y(|y|) / \Delta^6, \tag{6}$$

with the scalar functions $\delta_x, \delta_y: [0, \infty) \rightarrow [0, 1]$ defined as

$$\delta_x(|x|) = \begin{cases} \Delta^3 & |x| \in [0, x_m - \Delta) \\ 2|x|^3 + 3(\Delta - 2x_m)|x|^2 + 6x_m(x_m - \Delta)|x| + x_m^2(3\Delta - 2x_m) & |x| \in [x_m - \Delta, x_m] \\ 0 & |x| > x_m \end{cases} \tag{7}$$

and

$$\delta_y(|y|) = \begin{cases} \Delta^3 & |y| \in [0, y_n - \Delta) \\ 2|y|^3 + 3(\Delta - 2y_n)|y|^2 + 6y_n(y_n - \Delta)|y| + y_n^2(3\Delta - 2y_n) & |y| \in [y_n - \Delta, y_n] \\ 0 & |y| > y_n. \end{cases} \tag{8}$$

In particular, we have

$$\mathbf{v}(\mathbf{x}, t) = \begin{cases} \mathbf{u}(\mathbf{x}, t), & \mathbf{x} \in \mathcal{G}^0 \\ \mathbf{v}_L(\mathbf{x}, t), & \mathbf{x} \notin \text{interior}(\partial\mathcal{G}). \end{cases} \tag{9}$$

Proof: We seek the 2D, divergence-free linear velocity field

$$\mathbf{v}_L(x, y, t) = \mathbf{A}(t)\mathbf{x} + \mathbf{b}(t)$$

that is the closest to Eq. (1) in the C^0 norm over the grid G . Here,

$$\mathbf{A}(t) = \begin{pmatrix} a_{11}(t) & a_{12}(t) \\ a_{21}(t) & -a_{11}(t) \end{pmatrix}, \quad \mathbf{b}(t) = \begin{pmatrix} b_1(t) \\ b_2(t) \end{pmatrix}$$

are sought as continuous functions of time.

Specifically, for every t , we seek the matrix $\overline{\mathbf{A}}(t)$ and the vector $\overline{\mathbf{b}}(t)$ satisfying $(\overline{\mathbf{A}}, \overline{\mathbf{b}}) = \arg \min J(\mathbf{A}, \mathbf{b})$, $J(\mathbf{A}, \mathbf{b}) = \langle (a_{11}x + a_{12}y + b_1 - u_1)^2 + (a_{21}x - a_{11}y + b_2 - u_2)^2 \rangle$, with the average $\langle \cdot \rangle$ defined in Eq. (4). The minimum of the cost function $J(\mathbf{A}, \mathbf{b})$ satisfies

$$\frac{1}{2} \frac{\partial}{\partial a_{11}} J(\mathbf{A}, \mathbf{b}) = a_{11}[\langle x^2 \rangle + \langle y^2 \rangle] + [a_{12} - a_{21}]\langle xy \rangle + b_1\langle x \rangle - b_2\langle y \rangle - \langle xu_1 \rangle + \langle yu_2 \rangle = 0,$$

$$\frac{1}{2} \frac{\partial}{\partial a_{12}} J(\mathbf{A}, \mathbf{b}) = a_{11}\langle xy \rangle + a_{12}\langle y^2 \rangle + b_1\langle y \rangle - \langle yu_1 \rangle = 0,$$

$$\frac{1}{2} \frac{\partial}{\partial a_{21}} J(\mathbf{A}, \mathbf{b}) = a_{21}\langle x^2 \rangle - a_{11}\langle xy \rangle + b_2\langle x \rangle - \langle xu_2 \rangle = 0,$$

$$\frac{1}{2} \frac{\partial}{\partial b_1} J(\mathbf{A}, \mathbf{b}) = a_{11}\langle x \rangle + a_{12}\langle y \rangle + b_1 - \langle u_1 \rangle = 0,$$

$$\frac{1}{2} \frac{\partial}{\partial b_2} J(\mathbf{A}, \mathbf{b}) = a_{21}\langle x \rangle - a_{11}\langle y \rangle + b_2 - \langle u_2 \rangle = 0. \tag{10}$$

Now, by the symmetry condition equation (2), we have $\langle x \rangle = \langle y \rangle = \langle xy \rangle = 0$, and hence Eq. (10) simplifies to

$$a_{11} = \frac{\langle xu_1 \rangle - \langle yu_2 \rangle}{\langle x^2 \rangle + \langle y^2 \rangle}, \quad a_{12} = \frac{\langle yu_1 \rangle}{\langle y^2 \rangle}, \quad a_{21} = \frac{\langle xu_2 \rangle}{\langle x^2 \rangle},$$

$$b_1 = \langle u_1 \rangle, \quad b_2 = \langle u_2 \rangle,$$

which yields the C^0 -closest linear fit for $\mathbf{u}(\mathbf{x}, t)$ over the grid \mathcal{G} in the form of Eq. (5), as claimed in statement (i) of Theorem 1.

To prove statement (ii), we first note that Eq. (9) follows immediately from Eq. (6) based on the definition of the functions δ_x and δ_y in Eqs. (7) and (8). It only remains to show that \mathbf{v} is a class C^1 vector field.

As \mathbf{v} is piecewise smooth, we only need to show that it is continuously differentiable at the grid boundaries $\partial\mathcal{G}^0$ and $\partial\mathcal{G}$. This amounts to the requirement that $\delta_x(|x|)$ and $\delta_y(|y|)$ be class C^1 functions of their arguments.

If we write $\delta_x(x)$ in the more general parametric form

$$\delta_x(|x|) = \begin{cases} 1 & |x| \in [0, \alpha) \\ a|x|^3 + b|x|^2 + c|x| + d & |x| \in [\alpha, \beta] \\ 0 & |x| > \beta \end{cases} \tag{11}$$

for fixed constants $0 < \alpha < \beta < \infty$, then its continuous differentiability is equivalent to the conditions

$$\delta_x(\alpha) = 1, \quad \delta'_x(\alpha) = 0,$$

$$\delta_x(\beta) = 0, \quad \delta'_x(\beta) = 0,$$

or, equivalently,

$$a\alpha^3 + b\alpha^2 + c\alpha + d = 1, \quad a\beta^3 + b\beta^2 + c\beta + d = 0,$$

$$3a\alpha^2 + 2b\alpha + c = 0, \quad 3a\beta^2 + 2b\beta + c = 0.$$

The solution of this linear system of equations is given by

$$a = -2/(\alpha - \beta)^3, \quad b = 3(\alpha + \beta)/(\alpha - \beta)^3,$$

$$c = -6\alpha\beta/(\alpha - \beta)^3, \quad d = \beta^2(3\alpha - \beta)/(\alpha - \beta)^3. \tag{12}$$

The general form equation (11) will become relevant for our problem if we let

$$\alpha = x_m - \Delta, \quad \beta = x_m,$$

i.e., we set α to be the maximum x coordinate on the subgrid \mathcal{G}^0 , and set β to be the maximum x coordinate on the grid \mathcal{G} . Under this substitution, the parameter configuration equation (12) guaranteeing continuous differentiability for $\delta_x(x)$ becomes

$$a = 2/\Delta^3, \quad b = 3(\Delta - 2x_m)/\Delta^3,$$

$$c = 6x_m(x_m - \Delta)/\Delta^3, \quad d = x_m^2(3\Delta - 2x_m)/\Delta^3.$$

Using these parameters in Eq. (11), applying the rescaling $\delta_x \rightarrow \tilde{\delta}_x/\Delta^3$ and dropping the tilde leads to the expression

equation (7) in statement (ii) of Theorem 1. The proof for the expression equation (8) follows analogously by requiring continuous differentiability for $\delta_y(|y|)$.

Note that the above results extend directly to nonrectangular grids with the averaging operation in Eq. (4) appropriately modified.

C. Finite-domain FTLE algorithm

The FDFMLE algorithm we propose in this paper uses the trajectories of extended velocity field $\mathbf{v}(\mathbf{x}, t)$ [instead of those of $\mathbf{u}(\mathbf{x}, t)$] in the computation of the FTLE field $\sigma(t; t_0, \mathbf{x}_0)$. Specifically, we fix a small enough distance $\Delta > 0$ from the boundary of \mathcal{G} and compute the FTLE field associated with the differential equation

$$\dot{\mathbf{x}} = \mathbf{v}_L + (\mathbf{u} - \mathbf{v}_L) \delta_x(|x|) \delta_y(|y|) / \Delta^6. \tag{13}$$

The optimal choice of Δ depends on the application considered. Generally, Δ measures the inevitable small transition region around the boundary in which the original velocity field is altered. FTLE ridges reaching into this region will be altered because of the nontrivial value of the smoothing functions $\delta_x(x)$ and $\delta_y(y)$ in this region. This motivates us to choose Δ as small as possible. At the same time, if the original velocity field \mathbf{u} is strongly nonlinear and hence its C^0 distance from \mathbf{v}_L is relatively large, then selecting Δ small will create large gradients for Eq. (13) in the transition region, resulting in potential numerical difficulties.

Note that the FTLE field is a measure of the largest eigenvalue distribution of the Cauchy–Green strain tensor

$$\left[\frac{\partial \mathbf{x}(t; t_0, \mathbf{x}_0)}{\partial \mathbf{x}_0} \right]^T \frac{\partial \mathbf{x}(t; t_0, \mathbf{x}_0)}{\partial \mathbf{x}_0}$$

over the grid \mathcal{G} , and hence the FTLE field will be spatially homogeneous for any linear flow. As a result, the linear velocity field \mathbf{v}_L outside \mathcal{G} will not affect the ridges of the FTLE field computed for \mathbf{u} inside \mathcal{G}^0 .

By extending the flow outside \mathcal{G} to a linear velocity field that best matches the overall fluid motion inside \mathcal{G} , we allow for trajectories still inside \mathcal{G} to continue their separation and hence develop more pronounced FTLE ridges. At the same time, trajectories that have reached the boundary of the domain will “lock in” the FTLE ridges they have developed inside \mathcal{G} .

We conclude this section with an example of a steady analytic velocity field of the form

$$u = x - y^2, \quad v = -y + x^2. \tag{14}$$

This flow has two fixed points. The fixed point at (0,0) is a saddle point with an attached homoclinic orbit that surrounds the center point (1,1). The other branches of the stable and unstable manifolds of the saddle point are unbounded (cf. Fig. 1).

A forward-time FTLE analysis of the analytic flow is shown in Fig. 1(b). To obtain this result, we carried out FTLE without any restriction on the spatial domain. As a result, the full stable manifold is highlighted as a FTLE ridge.

We now restrict the FTLE computation artificially to the $[-6, 6] \times [-6, 6]$, pretending that no velocity data are available outside this square. Figure 1(c) shows the results of a FTLE calculation on this restricted domain with the trajectories stopped at the boundary. Note the well pronounced spurious LCS appearing at the right boundary. By contrast, Fig. 1(d) shows the results obtained from the FDFMLE algorithm proposed here. Note how this algorithm preserves the true LCS, while fully eliminating the spurious LCS. There is minor skewing of the stable manifold at the edge of the domain due to the transition between the original and the smoothly extended flows. Here the transition width was selected to be $\Delta = 1.5$. We discuss the choices of Δ in Sec. III with an example of a real flow.

III. APPLICATION: LCS OVER HONG KONG INTERNATIONAL AIRPORT

Here we consider the observational wind velocity data from coherent Doppler RADio Detection And Ranging (RADAR) and LIght Detection And Ranging (LIDAR) observations over HKIA. For such observational data sets, two constraints limit the straightforward extraction of LCS using the FTLE field equation (3). First, the LIDAR only measures the line-of-sight (LOS) velocity component relative to the instrument, and hence the cross-beam components of the velocity field are not directly available. Second, LIDAR observations have a limited range of detection outside of which the wind velocity remains unknown; this leads to edge effects and noise in LCS detection, as described in Sec. I.

We address the LOS constraint by employing variational wind retrieval techniques, while we handle the limited-domain problem using the FDFMLE technique developed in this paper.

A. Data set

We consider data from near-ground remote-sensing scans, which provide LOS velocities on a fixed 2D grid. The detection range of remote-sensing instruments is generally limited to the backscatter of signals. For the LIDAR system used at HKIA, the detection range is no more than 10 km in dry weather, and will shorten greatly in wet weather. The data coverage is also shortened during the standard retrieval procedure, resulting in a square domain of approximately 15 km on each side. To reconstruct the full velocity field within this domain, we use a modification of a two-step variational algorithm,⁴ as discussed by Chan and Shao.¹

This modified algorithm is currently in use by the Hong Kong Observatory for real-time monitoring of near ground winds near the airport. Overall, the reconstructed wind fields yield at least 0.9 correlation in wind speed and direction when compared with a set of independent anemometer measurements around the airport. Figure 2 shows both the measured LOS velocities as well as the reconstructed 2D velocity field.

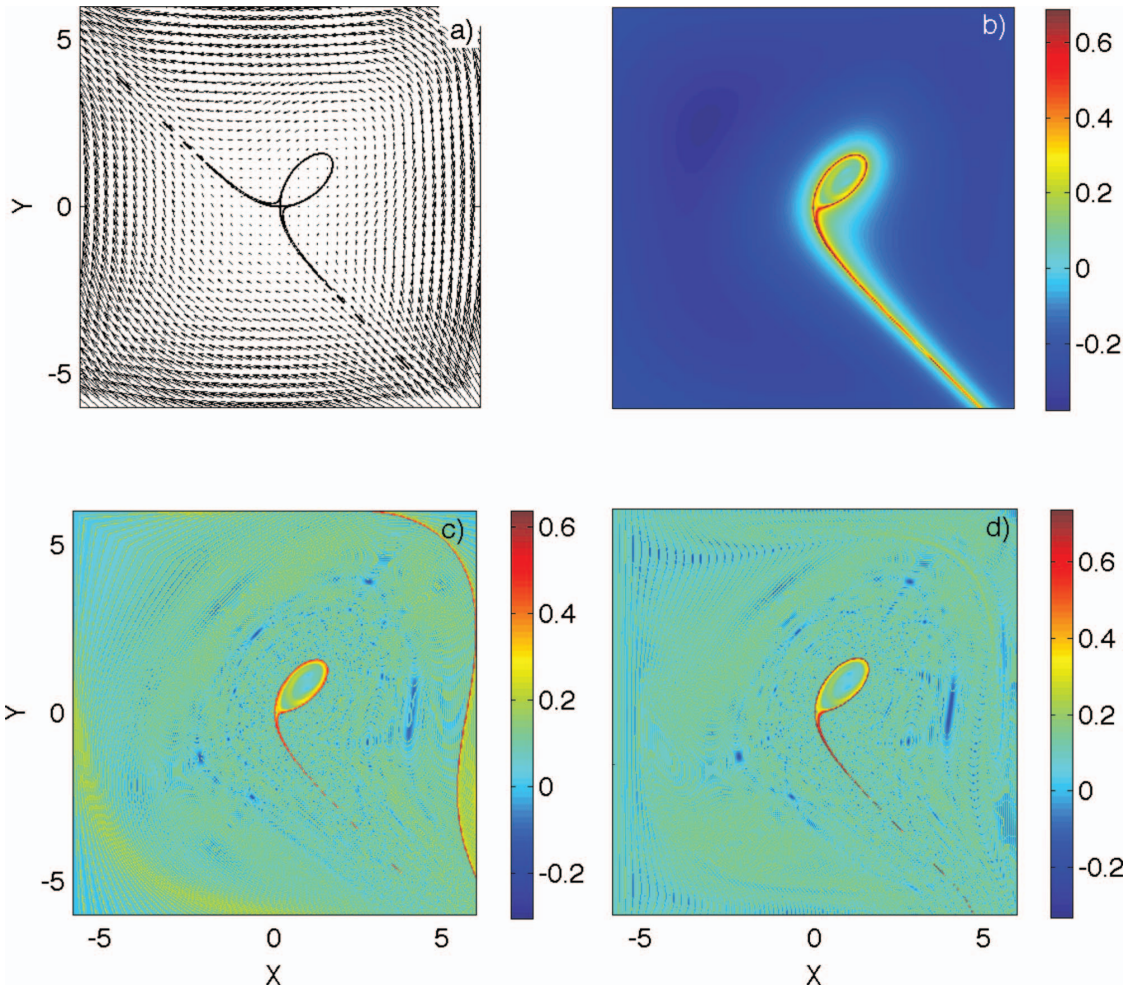


FIG. 1. (Color) (a) The velocity field of the idealized flow equation (14). The flow contains a homoclinic orbit and open branches of the stable and unstable manifolds. These manifolds are highlighted by the black trajectories. (b) Forward-time FTLE of the analytic flow revealing the full stable manifold. (c) FTLE distribution computed from the traditional technique which stops trajectories at the boundaries. An artificial ridge is introduced. (d) FDFTLTLE for the same flow, showing that the artificial structure is eliminated, and the true structures are retained.

Sector blanking is applied over the areas toward the south to southeast of the airport. LIDAR beam is also blocked by the air traffic control tower north of the LIDAR. Outliers due to clutters have already been removed from Fig. 2.

At the elevation angles of 1.4° and 3° that the LIDAR is scanning, the LIDAR beams cannot penetrate the mountains, hence data coverage is generally poor south of the airport, even outside of the sector blanking angles. The white contours in Fig. 2 indicate constant elevation of the terrain near

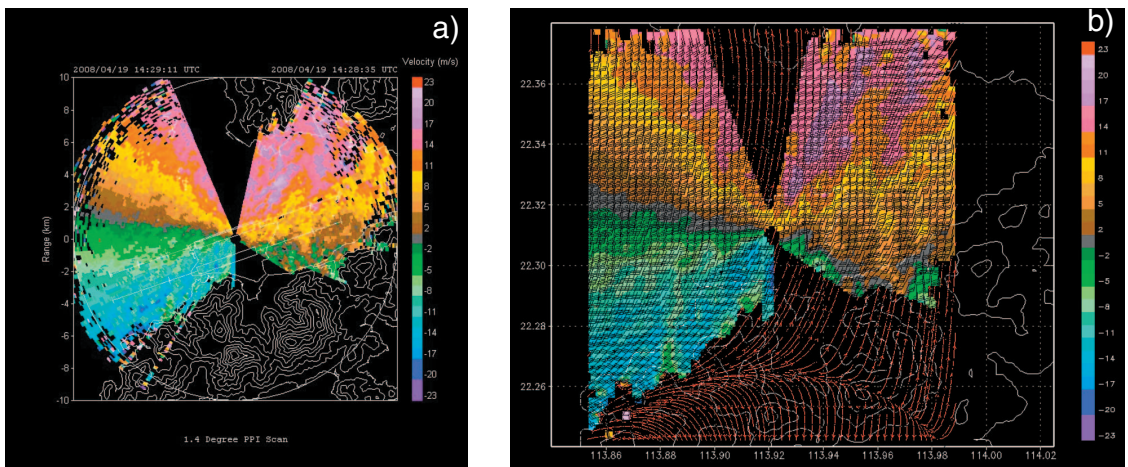


FIG. 2. (Color) (a) LOS velocity measured by a coherent Doppler LIDAR system at 1429 UTC, 19 April 2008, superimposed with contour plot of the terrain and runway strips of HKIA. Positive values indicate LOS velocity away from LIDAR. (b) Wind vectors and streamlines based on the reconstructed velocity at the same time.

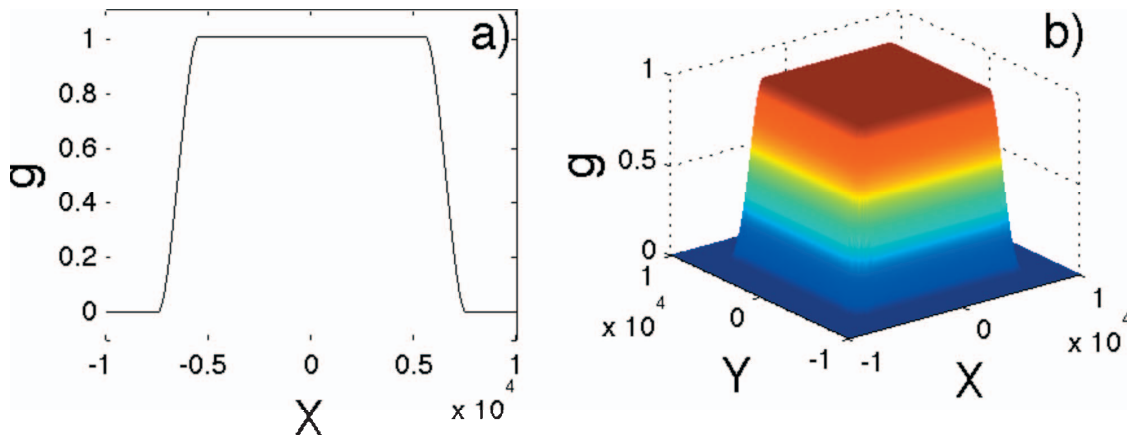


FIG. 3. (Color) Geometry of the bump function $\delta_x(|x|)\delta_y(|y|)$ used for the reconstructed wind field data over Hong Kong Airport.

the airport at 100 m intervals. The two runway strips are shown as white rectangles in the center of the plot, with runway corridors marked at the ends of the runways with tick marks at 1, 2, and 3 nautical miles away from the runway ends.

Figure 2(b) shows streamlines and wind vectors generated by the reconstruction technique discussed by Chan and Shao.¹ Wind velocities in the blocked regions are obtained from the same technique. The resulting velocity field can be treated roughly as 2D horizontal wind velocity near the surface.

B. Air disturbances and LCS

We seek to locate air disturbances that affect the landing and takeoff of commercial aircraft at the airport. These disturbances involve intense and localized air particle motion, and hence should be associated with LCS. We wish to locate LCS as ridges of the FTLE field defined in Eq. (3).

Specifically, ridges of the forward-time FTLE field correspond to repelling LCS in the near-ground 2D scans. These translate to downdrafts for the full three-dimensional wind field. Similarly, ridges of the backward-time FTLE field correspond to attracting LCS in the 2D scan, which indicate the presence of updrafts in the full wind field.

To obtain either FTLE field, air particle trajectories need to be generated by integration of a grid of initial conditions under the reconstructed velocity field. For trajectories starting near the down-wind end of the domain, separation or attraction is unaccounted for once they leave the square domain of the data set. Instead of following standard practice and stopping trajectory integration at the boundary of the domain, we use the FDFTLE technique to eliminate spurious FTLE ridges and enhance true FTLE ridges within the observational domain.

In this study, we choose $\Delta=2$ km for the transition region width. Figure 3 shows the bump function g in the x -direction (a) and in the x,y -plane (b). In general, increasing Δ results in loss of coherent structures inside the domain, whereas decreasing Δ results in a quick transition between the interior and exterior flows, resulting in strong velocity gradients that are accompanied with spurious structures.

These spurious structures can be suppressed by appropriate choices of Δ through visual inspection. The transition region between \mathcal{G}^0 and \mathcal{G} chosen above is small relative to the overall size of the observational domain, yet not too small to introduce numerically intractable gradients.

Figure 4 shows a comparison between LCS extracted with no-slip boundary conditions and LCS extracted using the FDFTLE algorithm at 1429 Coordinated Universal Time (UTC), 19 April 2008. The black contours are constant elevations of the terrain at 100 m intervals. The airflow enters the domain from the southwest corner and exit from the northeast. Coherent structures arise from airflow past the mountains south of the airport. Some structures appear in the mountain regions where there is no LIDAR coverage. They do not affect the flight data analyses as they do not intersect with the flight path at the end of trajectory integration.

A crucial improvement obtained from the FDFTLE algorithm is the recovery of the underestimated LCS marked by “B” in Fig. 4(b). The underestimation is due to trajectories stopped at the boundaries before the end of integration; for these trajectories, exponential separation is stopped prematurely. The LCS denoted by B highlights a region of potential hazard that is missing in Fig. 4(a).

In addition, several spurious blue structures in Fig. 4(a) have been removed by the FDFTLE algorithm. Again, these ridges in the FTLE field were originally separators between initial conditions terminating at different no-slip boundary components at different times.

Furthermore, at the right edge of Fig. 4(a), several spurious ridges around the region marked by “A” disappear under the FDFTLE algorithm. These ridges highlight spurious separatrices between initial conditions that leave the domain through the right boundary and stop, and others that continue their flight and leave the boundary through the top.

Some of the spurious structures turn out to be on the flight path to be analyzed below. As we noted earlier, automated feature extraction and decision making are only possible using LCS extraction if such artificial ridges are discounted, a requirement that the present FDFTLE analysis does satisfy.

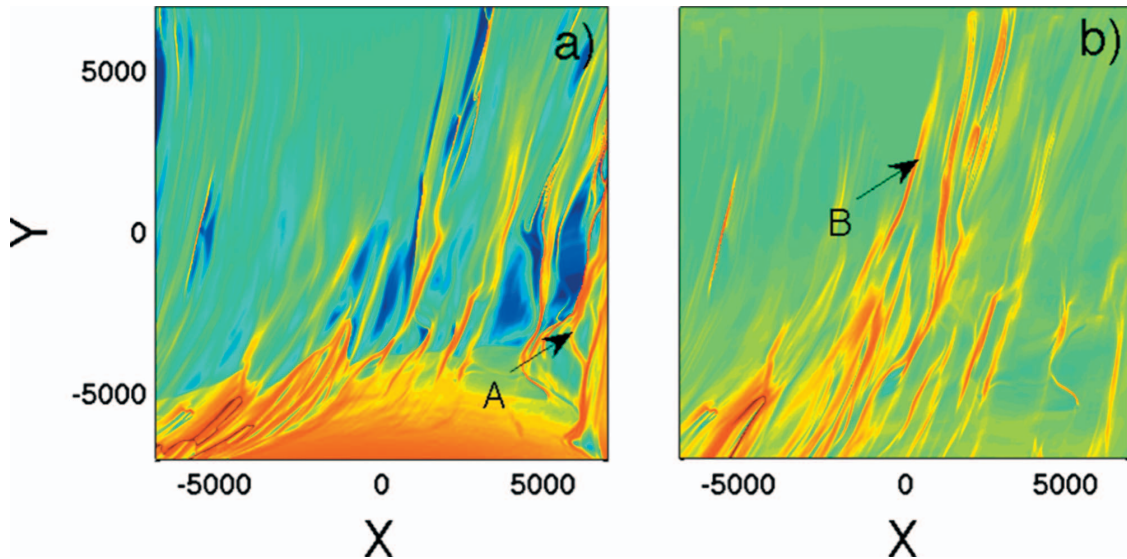


FIG. 4. (Color) Comparison between LCSs obtained from two trajectory integration schemes. Black contours are constant elevations at 100 m intervals. (a) Forward-time FTLE with trajectory integration stopped at the boundary of the data domain. A few spurious structures are marked by A. (b) Forward-time FDFMLE developed in this paper. Note that a LCS (B) originally suppressed by the high values of spurious FTLE ridges is now recovered. Some spurious structures appear in the mountains where LIDAR measurements are not available. They are ignored in the flight data analyses as they are not on the flight path.

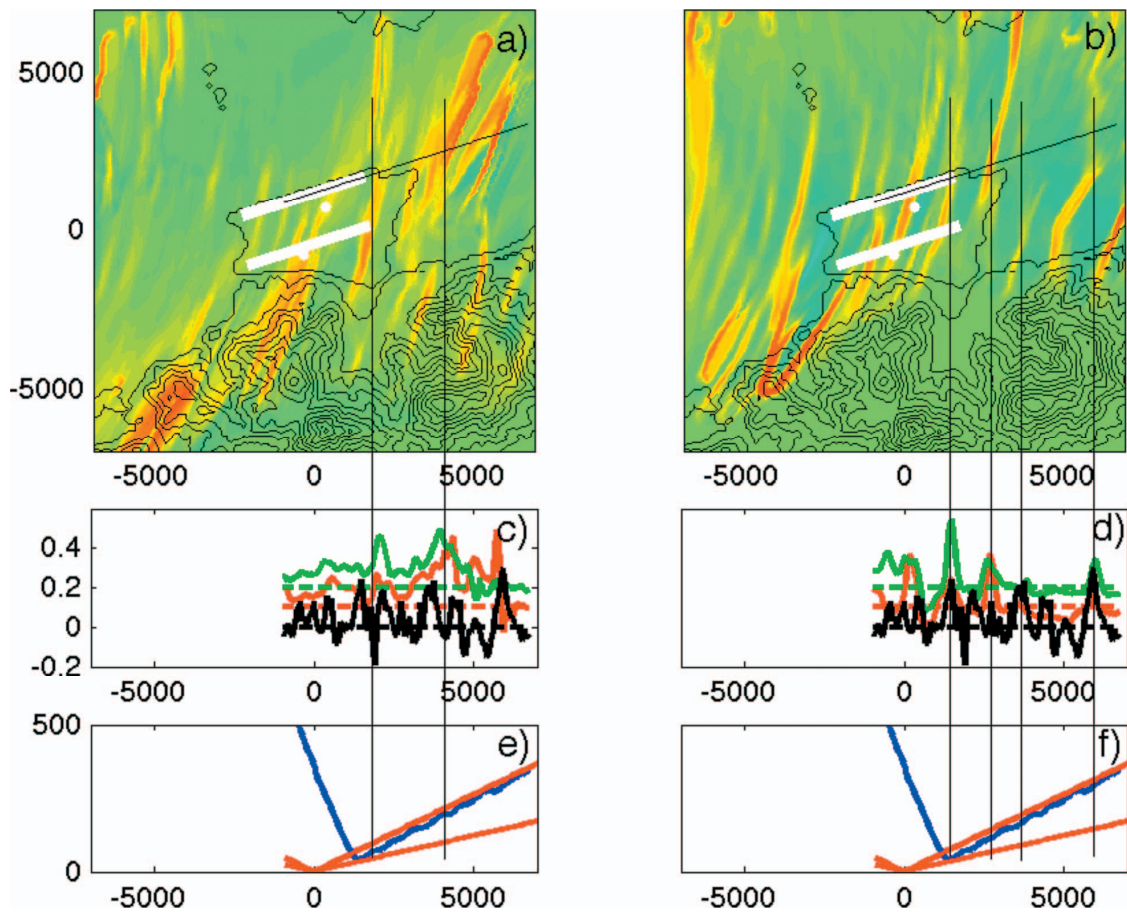


FIG. 5. (Color) Comparison between LCS and on-board estimates of vertical wind velocity during a missed approach on 19 April 2008. Top panels: the color maps indicate values of the FDFMLE fields. The white rectangles in the center of the domain are the runway strips; the flight path is aligned with the northern runway strip as black lines. Black isocontours are the topography near HKIA shown at 100 m intervals. (a) Forward-time FDFMLE. (b) Backward-time FDFMLE. Center panels: vertical velocity estimates (scaled down by 20 for convenience of comparison) are shown as the black curves, with the dashed line corresponding to zero vertical velocity. The red and green curves correspond to FDFMLE interpolated on the flight path from 1.4° and 3.0° scans of the LIDAR, respectively. These two curves are shifted to allow direct comparison between peaks and troughs. The zero values are shown as the dashed red and green lines. (c) Forward-time FDFMLE. (d) Backward-time FDFMLE. The bottom panels are the landing altitudes (blue) and the location of the LIDAR scanning angles (red). The black vertical lines throughout different panels highlight the coincidence of updrafts and downdrafts sensed by the on-board instruments with LCS reconstructed from LIDAR observations.

C. Impact of LCS on landing of aircraft

Recall that the observational domain is a square of approximately 15×15 km². A typical landing aircraft will spend the last 70–80 s of its flight in this square domain before touchdown.

We use LCS extracted by the FDFTLE method to interpret the flow structures around the airport and infer different types of threats to actual flights. To verify the relevance of LCS obtained from the FDFTLE method, we compare the LCS interpolated along a flight path with actual recordings of wind experienced by the aircraft flying on that path.

Figure 5 illustrates a comparison between the forward-time and backward-time FDFTLE fields, and on-board estimates of vertical wind velocity and altitude during an aborted landing attempt by an unidentified aircraft on 19 April 2008. The airplane landed safely during a second attempt.

The top panels [Figs. 5(a) and 5(b)] correspond to the FDFTLE field obtained from the 1.4° LIDAR scan. The white rectangles in the center of the domain are the runway strips and the two white dots are locations of the HKIA LIDARs. The straight black lines aligned with the northern runway in each panel indicate the airplane path. The airplane entered the observational domain \mathcal{G} from the right boundary and approached the airport located in the middle of the domain. The airplane path does not extend over the runway threshold at HKIA since the aircraft continues to record data after it pulls up from descent.

The center panels [Figs. 5(c) and 5(d)] show the vertical velocity estimated from on-board sensors (black) with forward- and backward-time FDFTLE fields interpolated along the flight path. The red curves are obtained from 1.4° scans and the green curves are obtained from 3.0° scans. The bottom panels [Figs. 5(e) and 5(f)] show the airplane altitude as it approaches the runway threshold (blue curve). The two red curves indicate LIDAR cones at 1.4° and 3.0°.

We draw vertical lines to align different FDFTLE peaks with vertical wind velocity and find that there is a close match between peaks in forward-time FDFTLE and downdrafts as well as peaks in backward-time FDFTLE and updrafts. Note that we identify updrafts and downdrafts based on on-board measurements, while we extract LCS independently from LIDAR observations.

Unexpected updrafts and downdrafts interfere with the landing of the aircraft and may lead to a missed approach, as in the example discussed above. The high correlation between these disturbances and LCS is promising: it suggests that after appropriate FDFTLE processing, ground-based LIDAR observations may be used for the real-time detection of

aerial features that potentially thwart a landing attempt. Note that these features will remain invisible in a radar scan if they have no significant moisture content.

IV. CONCLUSIONS

We have described an algorithm for extracting LCSs from velocity fields localized over a small spatial domain. The algorithm locates LCS as ridges of a FTLE field computed for an extension of the original velocity field to the whole 2D plane. The extension is smooth and linear outside the original domain of the data; this linearity guarantees that no spurious FTLE ridges are introduced by the extension.

We illustrated the use of this technique in the analysis of the wind data along the flight paths at the HKIA based on LIDAR measurements of the wind field and on-board measurements of the vertical wind velocity and the altitude. We have shown how the FDFTLE technique discounts spurious ridges resulting from the stopping of trajectory integration at the original observational domain boundary. We have also demonstrated that FDFTLE recovers some of the true LCSs suppressed by strong spurious ridges of the original FTLE field.

A comparison of LCS to on-board estimation of disturbances shows that the FDFTLE scheme captures unexpected disturbances to the planned flight path without introducing false alarms, or missing some of the LCSs. In our experience, detection is more accurate when the airplane is closer to the ground, as LCSs are more likely to be induced by vertical motion than by pure horizontal motion.

A three-dimensional extension of the current technique is straightforward, although the resulting formulas are more complicated. A more detailed analysis of hazard detection near HKIA using FDFTLE techniques will appear elsewhere.

ACKNOWLEDGMENTS

The authors would like to thank Cathay Pacific Airways for the supply of flight data with agreement of the Hong Kong Aircrew Officers Association (HKAOA). They also thank two anonymous referees for their helpful comments.

¹Chan, P. W. and Shao, A. M., “Depiction of complex airflow near Hong Kong International Airport using a Doppler LIDAR with a two-dimensional wind retrieval technique,” *Meteorol. Z.* **16**, 491–504 (2007).

²Haller, G., *Chaos Near Resonance* (Springer, New York, 1999), p. 448.

³Haller, G., “Distinguished material surfaces and coherent structures in three-dimensional fluid flows,” *Physica D* **149**, 248–277 (2001).

⁴Qiu, C. J., Shao, A. M., Liu, S., and Xu, Q., “A two-step variational method for three-dimensional wind retrieval from single Doppler radar,” *Meteorol. Atmos. Phys.* **91**, 1–8 (2006).

⁵Shadden, S. C., Lekien, F., and Marsden, J. E., “Definition and properties of Lagrangian coherent structures from finite-time Lyapunov exponents in two-dimensional aperiodic flows,” *Physica D* **212**, 271–304 (2005).